Single-nanoparticle detection with slot-mode photonic crystal cavities

Cheng Wang, Qimin Quan, Shota Kita, Yihang Li, and Marko Lončar

---

Articles you may be interested in

Single-nanoparticle detection with slot-mode photonic crystal cavities

Cheng Wang,[1] Qimin Quan,[2] Shota Kita,[1] Yihang Li,[1,3] and Marko Lončar[1,a]

[1]School of Engineering and Applied Sciences, Harvard University, Cambridge, Massachusetts 02138, USA
[2]Rowland Institute at Harvard University, Cambridge, Massachusetts 02142, USA
[3]Department of Electronic Engineering, Tsinghua University, Beijing 100084, People's Republic of China

Optical cavities that are capable for detecting single nanoparticles could lead to great progress in early stage disease diagnostics and the study of biological interactions on the single-molecule level. In particular, photonic crystal (PhC) cavities are excellent platforms for label-free single-nanoparticle detection, owing to their high quality (Q) factors and wavelength-scale modal volumes. Here, we demonstrate the design and fabrication of a high-Q ($>10^4$) slot-mode PhC nanobeam cavity, which is able to strongly confine light in the slotted regions. The enhanced light-matter interaction results in an order of magnitude improvement in both refractive index sensitivity (439 nm/RIU) and single-nanoparticle sensitivity compared with conventional dielectric-mode PhC cavities. Detection of single polystyrene nanoparticles with radii of 20 nm and 30 nm is demonstrated in aqueous environments (D_2O), without additional laser and temperature stabilization techniques. © 2015 AIP Publishing LLC. [http://dx.doi.org/10.1063/1.4923322]

Label-free optical biosensors have proven to be a powerful tool for clinical diagnostics and biomedical research since they are noninvasive and easy to implement.[1,2] In the past decade, optical micro- and nano-cavities, with high quality (Q) factors and small modal volumes (V_m), have pushed the sensitivity limit to the level of single nano-objects.[3–15] In particular, whispering-gallery-mode (WGM) resonators such as μ-spheres, μ-disks, and μ-rings have been extensively explored, and detection of single nanoparticles and viruses has been demonstrated on these platforms.[3–9] The ultimate single-nanoparticle detection limit of resonant-type optical biosensors is determined by Q/V_m, which is usually a constant for WGM resonators in radiation-loss-limited cases. To break this Q/V_m limitation, hybrid photonic-plasmonic systems have been proposed to leverage the strong field confinements from localized plasmons. Using this method, single protein detection has been achieved[10] and the study of nucleic acid interactions on the single-molecule level was demonstrated.[11]

On the other hand, photonic crystal (PhC) cavities have emerged as a powerful alternative for applications that require strong light confinements.[12–21] Theoretically, PhC cavities could achieve a similar level of Q factors as WGM resonators, but with much smaller V_m.[22] In the past few years, promising results on single-nanoparticle sensing, trapping, and manipulation based on PhC cavities have been reported.[12–15] However, almost all conventional PhC cavities are operating in dielectric modes, where most of the electromagnetic energy is confined in the dielectric regions.[23] In this case, light-matter interactions that often take place in the lower index regions (e.g., air or water) could only be accessed by evanescent fields, degrading the system performances. Meanwhile, it has been shown that additional nano-slots in dielectric cavities could significantly enhance the optical field intensities in those regions while maintaining tight light confinements.[24] Using this approach, enhanced system performances in applications including optical trapping,[13] biosensing,[25] and quantum optics[26] have been reported.

Herein, we demonstrate the design, fabrication, and characterization of a high-Q slot-mode PhC nanobeam cavity, as well as its applications in single nanoparticle sensing. Our slot-mode cavities possess experimental Q factors $\sim 1.2 \times 10^4$ with $V_m \sim 0.06$ $(\lambda/n_{water})^3$. Enhanced light-matter interaction results in a high refractive index sensitivity of 439 nm per refractive index unit (RIU). Moreover, we demonstrate the detection of single polystyrene (PS) nanoparticles with radii of 20 and 30 nm in aqueous environment, with responses almost an order of magnitude stronger than a typical non-slot PhC cavity.[15] We estimate a detection limit that corresponds to 14 nm radius PS nanoparticles, which is similar to two recent reports using WGM resonators.[8,9]

The structure of the proposed slot-mode PhC nanobeam cavity is shown in Fig. 1(a). Rectangular air slots are placed between adjacent circular air holes. The PhC period a, beam width w, beam thickness t, and air hole radius r are fixed, while the slot width s is quadratically tapered from an initial value to zero over the modulated mirror section. In comparison with previously reported designs with slot width fixed throughout the device,[27] our configuration offers a larger bandgap for mirror modes since at the end of the modulated section, the structure gradually turns to a conventional PhC without air slots. Therefore, it gives more robustness in fabrication and the possibility to design devices in an asymmetric environment, i.e., the device (made of silicon) is placed on top of silicon dioxide and immersed in water. Fig. 1(b) shows the transverse-electric (TE) band diagrams for the designed PhC with and without slot, which correspond to cavity and mirror modes, respectively. 3D finite-difference time-domain (FDTD) simulation results (E_y) of the proposed structures are displayed in the inset of Fig. 1(c), showing field enhancement inside the air slots enforced by the

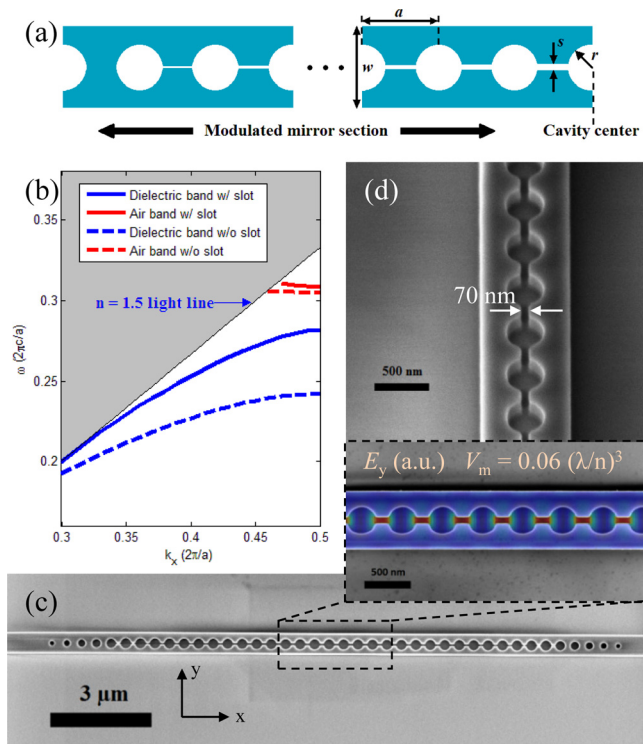a)Author to whom correspondence should be addressed. Electronic mail: loncar@seas.harvard.edu

FIG. 1. (a) Schematic of the slot-mode PhC cavity. PhC period a, beam width w, beam thickness t, and air hole radius r are fixed, while air slot width s is quadratically tapered to zero throughout the modulated mirror section. (b) Band diagrams of the proposed PhC structures with air slot width s (solid curves) and without air slot (dashed curves), representing PhC modes at the cavity center and at the end of the mirror section, respectively. The structure parameters are chosen as: $w = 1.442a$, $r = 0.349a$, and $t = 0.512a$. The slot width s is quadratically tapered from $0.163a$ to 0. (c) SEM image of a representative cavity with 15 mirror pairs. Inset shows a magnified view of the cavity center region, together with simulated E_y field distribution. (c) SEM image showing smooth and vertical etching profile in the slots with width $\sim$70 nm, taken at a 30° angle.

electromagnetic boundary conditions. With 15 mirror pairs, the simulated Q factor and V_m are 600 000 and 0.06 $(\lambda/n_{water})^3$, respectively.

The period a of the actually fabricated devices is chosen to be 430 nm so that the operating wavelength lies in the telecom wavelength range. The slot width s is quadratically tapered from $0.163a$ (70 nm) to 0. Other structural parameters are accordingly chosen as: beam width $w = 1.442a = 620$ nm, hole radius $r = 0.349a = 150$ nm, and beam thickness $t = 0.512a = 220$ nm. Starting from silicon-on-insulator (SOI) substrates, with 220 nm thick Si on top of 2 μm thick buried oxide, the devices were fabricated using a combination of electron-beam lithography (EBL) and reactive ion etching (RIE). Hydrogen silsesquioxane (HSQ) based electron-beam resist (XR-1541, Dow Corning) was patterned on top of the SOI using EBL (ELS-F125, Elionix) and used as the etching mask for the subsequent RIE, which was performed with C_4F_8 and SF_6 gases using an STS ICP-RIE. Correction on the electron-beam dosage was applied using Layout BEAMER software (GenISys) to eliminate proximity effects so that narrow, straight, and clear slots could be obtained. Figs. 1(c) and 1(d) show scanning electron microscope (SEM) images of a representative device with 15 mirror pairs of air holes with slot widths tapering from 70 nm in the center to 0 at the end of the cavity. A second EBL was performed to define

SU-8 input/output couplers to convert the waveguide modes to and from lensed fibers in a similar manner as in our previous report.[19]

Transmission spectra of the devices were measured using a tunable telecom laser source (TSL-510, Santec) and an InGaAs near infrared photodetector (IGA1.9-010-H, EO Systems). Samples were treated with oxygen plasma to create a hydrophilic surface, and were cleaved such that the SU-8 couplers on chip were exposed on the edges. Light from the tunable laser was coupled into and collected from the SU-8 couplers through tapered lensed fibers (OZ optics). An inline fiber polarizer was used to control the polarization of input light. The desired device environment was introduced by dripping certain solutions on top of the devices. Between each experiment, the sample was thoroughly cleaned in solvents with sonication and treated with oxygen plasma. All of the following experiments were performed on the same cavity to ensure data reliability, and we did not observe noticeable resonance wavelength shifts and/or Q factor degradations due to the cleaning processes.

Fig. 2(a) shows a representative TE transmission spectrum of a device immersed in heavy water (D_2O), which possesses lower absorption loss in telecom wavelengths than normal water. Three transmission peaks could clearly be identified, which correspond to longitudinal modes with 1st, 2nd, and 3rd orders. Fig. 2(b) shows a magnified view of the fundamental mode, which has the highest Q factor and the smallest V_m. Lorentzian fit of the transmission peak indicates a measured Q factor of 12 000. The discrepancy in Q values between simulation and experiment is attributed to the fact that slots with widths less than 40 nm could not be etched vertically and thoroughly, which disturbs the ideal band-structure shifts at the end of the modulated mirror regions and induces more scattering losses. If operating in normal water, the absorption loss would limit the Q factor <6000. In fact, devices operating in air could also be realized using the
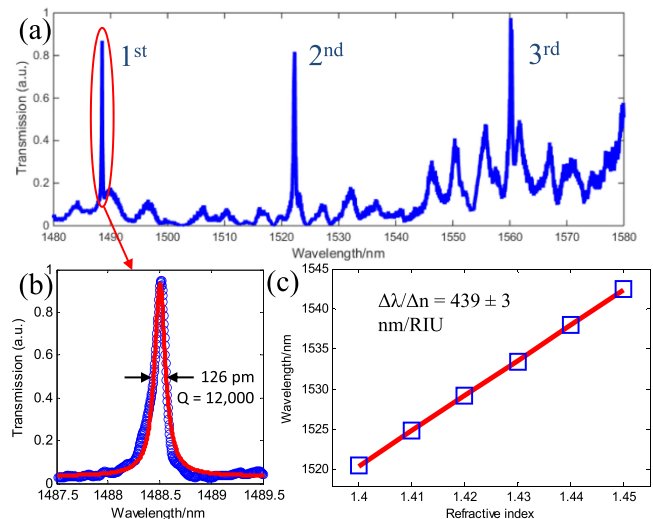

FIG. 2. (a) Transmission spectrum of a representative slot-mode PhC nanocavity immersed in D_2O, showing three different modes. (b) Magnified view of the fundamental (1st) mode in (a) together with its Lorentzian fit (red curve), indicating a Q factor of 12 000. (c) Measured fundamental mode wavelengths in standard refractive index liquids ($n = 1.40$–1.45). Linear fit (red line) of the data shows a refractive index sensitivity of 439 ± 3 nm/RIU.

same design principle, where the index asymmetry between top ($n = 1$) and bottom ($n = 1.5$) is even stronger, and we have experimentally achieved similar level of Q factors in such devices (data not shown). We characterized the refractive index sensitivity of our devices by measuring the fundamental mode wavelengths in certified refractive index liquids (Cargille Labs) with refractive indices from 1.40 to 1.45 (Fig. 2(c)). Linear fit of the data shows an index sensitivity of 439 ± 3 nm/RIU, much higher than a typical non-slot nanobeam cavity (83 nm/RIU)[15] due to the strong light localization in the slotted regions. Our simulation confirmed that the fundamental mode wavelength shifts continuously and linearly with environmental refractive indices, and the theoretical sensitivity (430 nm/RIU) also matches with the measured value well. The index sensitivity could be further enhanced by removing the residue electron-beam resist on top of Si (usually $\sim$50 nm thick). In the case of single nanoparticle sensing discussed next, however, the remaining resist could indeed reduce unwanted noise from particles attached to the device top surface.

Next, we characterized the nanoparticle sensing performance of our slot-mode PhC cavities by introducing droplets of solutions dissolved with PS nanoparticles on top of the devices. Cavity resonance was monitored over time by sweeping the tunable laser continuously. Resonance wavelengths for each sweep were determined by Lorentzian fitting. We start with solutions containing PS nanoparticles with 30 nm radius ($\sim$1 pm). Fig. 3(a) shows the corresponding resonance wavelength change over time, indicating clear cavity resonance "jumps" as nanoparticles approach and leave the cavity by Brownian motion, possibly assisted by optical trapping force as well. The step heights for different "jump" events are on a similar scale, but slightly differ from each other, since the particles could land on different slots and on different areas of the slots. As a comparison, in the case of 20 nm radius PS nanoparticles, the "jump" steps are

significantly smaller due to reduced perturbation to the cavity (Fig. 3(b)). When no nanoparticles are present, no distinguishable "jump" events were recorded (Fig. 3(c)). To quantitatively analyze the particle-induced resonance shifts in each case, we calculated the differential shift, defined as the resonance wavelength difference (absolute value) between consecutive scans (Figs. 3(d)–3(f)). The 3σ noise level ($\sim$0.4 pm) in Fig. 3(f) were taken as reference and plotted as the red bars, and all data points above the 3σ level in Figs. 3(d) and 3(e) therefore refer to "jump" events. The baseline noise when absent of particles is attributed to laser and/or temperature fluctuations. The average step heights for 30 nm and 20 nm radius nanoparticles are 2.42 pm and 1.07 pm, respectively. Compared with previous results in conventional non-slot nanobeam cavities ($\sim$0.27 pm resonance shift with 25 nm PS nanoparticles),[15] responses from our slot-mode cavities are almost an order of magnitude higher due to the slot-induced field enhancement. According to perturbation theory, the resonance shift is proportional to the excess polarizability (thus volume) of the nanoparticles if they appear at the same location (field maximum here).[23] In our experiments, the measured response from 20 nm nanoparticles is 44% of that from 30 nm nanoparticles, while the volume of the former is around 30% of the latter. This is possibly because smaller particles could move closer to the slot surface, where electromagnetic field is the strongest. We use the measured single-nanoparticle response (1.07 pm) from 20 nm particles and noise level (0.4 pm) to estimate the upper bound of our detection limit, which corresponds to a radius of 14 nm for PS nanoparticles.

In conclusion, we have demonstrated a slot-mode PhC nanobeam cavity, which does not require free-standing structures and is ideal for applications in aqueous environments. The proposed cavities possess experimental Q factors $\sim$12 000, which represent the highest measured value in similar slotted configurations.[21,27] Moreover, our cavities provide strong light confinement in the slotted regions with V_m as low as 0.06 $(\lambda / n_{water})^3$, boosting their performance in sensing applications. The measured refractive index sensitivity is 439 ± 3 nm/RIU, more than 5 times better than a typical non-slot nanobeam cavity.[15] We performed nanoparticle sensing experiments, which show clear "jump" events from single PS nanoparticles with radii of 20 and 30 nm. From the single nanoparticle response and our experimental noise level, we estimated the upper bound of our detection limit to be corresponding to 14 nm radius PS nanoparticles, which is on the same level of two recent reports using WGM resonators.[8,9] It has to be mentioned that our devices are fabricated on standard SOI platforms and are CMOS compatible. A simple approach to improve the detection limit is to reduce the noise of our system (e.g., detector noise and setup vibration) as well as to improve the stability of our laser. The detection limit could be further improved by an order of magnitude if the system is scaled down to operate in visible wavelengths using silicon nitride or other materials with large bandgaps, which would enable real-time detection of single proteins and monitoring of single-protein interactions without plasmonic enhancement. This would also allow such experiments to be operated in normal water due to lowered
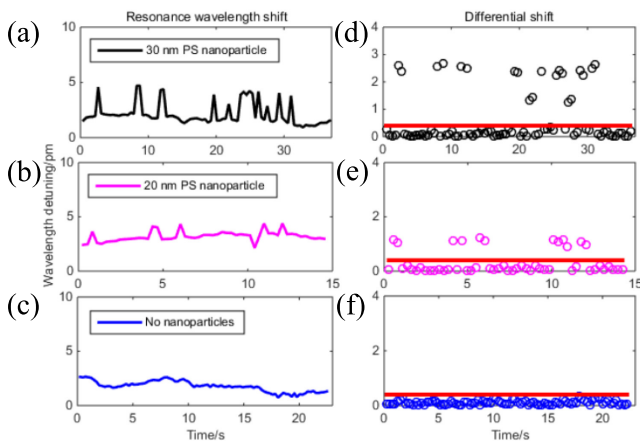

FIG. 3. Single nanoparticle sensing results in solutions with 30 nm PS nanoparticles ((a) and (d)), 20 nm PS nanoparticles ((b) and (e)), and without nanoparticles ((c) and (f)). (a)–(c) Cavity resonance wavelength (obtained from Lorentzian fits of each sweep) shift in real time. Clear "jump" events can be identified when nanoparticles are present in the device environment. (d)–(f) Differential shift (resonance wavelength difference between consecutive sweeps) in real time showing the step height of each "jump" event. Red bars show the 3σ ($\sim$0.4 pm) level in the control experiment (no nanoparticles).

absorption in these wavelengths, which is more feasible for biological sensing applications.

[1]X. Fan, I. M. White, S. I. Shopova, H. Zhu, J. D. Suter, and Y. Sun, Anal. Chim. Acta **620**(1–2), 8–26 (2008).

[2]F. Vollmer and L. Yang, Nanophotonics **1**(3–4), 267 (2012).

[3]F. Vollmer, S. Arnold, and D. Keng, Proc. Natl. Acad. Sci. U.S.A. **105**(52), 20701–20704 (2008).

[4]J. Zhu, S. K. Ozdemir, Y. F. Xiao, L. Li, L. He, D.-R. Chen, and L. Yang, Nat. Photonics **4**(1), 46–49 (2010).

[5]L. He, S. K. Ozdemir, J. Zhu, W. Kim, and L. Yang, Nat. Nanotechnol. **6**(7), 428–432 (2011).

[6]T. Lu, H. Lee, T. Chen, S. Herchak, J.-H. Kim, S. E. Fraser, R. C. Flagan, and K. Vahala, Proc. Natl. Acad. Sci. U.S.A. **108**(15), 5976–5979 (2011).

[7]L. Shao, X. F. Jiang, X.-C. Yu, B.-B. Li, W. R. Clements, F. Vollmer, W. Wang, Y. F. Xiao, and Q. Gong, Adv. Mater. **25**(39), 5616–5620 (2013).

[8]B. B. Li, W. R. Clements, X. C. Yu, K. Shi, Q. Gong, and Y. F. Xiao, Proc. Natl. Acad. Sci. U.S.A. **111**(41), 14657–14662 (2014).

[9]Ş. K. Özdemir, J. Zhu, X. Yang, B. Peng, H. Yilmaz, L. He, F. Monifi, S. H. Huang, G. L. Long, and L. Yang, Proc. Natl. Acad. Sci. U.S.A. **111**(37), E3836–E3844 (2014).

[10]V. R. Dantham, S. Holler, C. Barbre, D. Keng, V. Kolchenko, and S. Arnold, Nano Lett. **13**(7), 3347–3351 (2013).

[11]M. D. Baaske, M. R. Foreman, and F. Vollmer, Nat. Nanotechnol. **9**(11), 933–939 (2014).

[12]S. Mandal, X. Serey, and D. Erickson, Nano Lett. **10**(1), 99–104 (2010).

[13]Y. F. Chen, X. Serey, R. Sarkar, P. Chen, and D. Erickson, Nano Lett. **12**(3), 1633–1637 (2012).

[14]S. Lin and K. B. Crozier, ACS Nano **7**(2), 1725–1730 (2013).

[15]Q. Quan, D. L. Floyd, I. B. Burgess, P. B. Deotare, I. W. Frank, S. K. Y. Tang, R. Ilic, and M. Lončar, Opt. Express **21**(26), 32225–32233 (2013).

[16]Y. Akahane, T. Asano, B. S. Song, and S. Noda, Nature **425**(6961), 944–947 (2003).

[17]P. B. Deotare, M. W. McCutcheon, I. W. Frank, M. Khan, and M. Lončar, Appl. Phys. Lett. **94**(12), 121106 (2009).

[18]M. Eichenfield, J. Chan, R. M. Camacho, K. J. Vahala, and O. Painter, Nature **462**(7269), 78–82 (2009).

[19]P. B. Deotare, I. Bulu, I. W. Frank, Q. Quan, Y. Zhang, R. Ilic, and M. Lončar, Nat. Commun. **3**, 846 (2012).

[20]J. D. Thompson, T. G. Tiecke, N. P. de Leon, J. Feist, A. V. Akimov, M. Gullans, A. S. Zibrov, V. Vuletić, and M. D. Lukin, Science **340**(6137), 1202–1205 (2013).

[21]D. Yang, S. Kita, F. Liang, C. Wang, H. Tian, Y. Ji, M. Lončar, and Q. Quan, Appl. Phys. Lett. **105**(6), 063118 (2014).

[22]Q. Quan and M. Loncar, Opt. Express **19**(19), 18529–18542 (2011).

[23]J. D. Joannopoulos, S. G. Johnson, J. N. Winn, and R. D. Meade, *Photonic Crystals: Molding the Flow of Light* (Princeton University Press, 2011).

[24]J. T. Robinson, C. Manolatou, L. Chen, and M. Lipson, Phys. Rev. Lett. **95**(14), 143901 (2005).

[25]S. Kita, S. Hachuda, S. Otsuka, T. Endo, Y. Imai, Y. Nishijima, H. Misawa, and T. Baba, Opt. Express **19**(18), 17683–17690 (2011).

[26]A. Goban, C. L. Hung, S. P. Yu, J. D. Hood, J. A. Muniz, J. H. Lee, M. J. Martin, A. C. McClung, K. S. Choi, D. E. Chang, O. Painter, and H. J. Kimble, Nat. Commun. **5**, 3808 (2014).

[27]J. D. Ryckman and S. M. Weiss, Appl. Phys. Lett. **101**(7), 071104 (2012).